

Research Article

Study on Nanostructures Induced by High-Current Pulsed Electron Beam

Bo Gao, Yi Hao, Ganfeng Tu, and Wenyuan Wu

School of Materials and Metallurgy, Northeastern University, Shenyang, Liaoning 110004, China

Correspondence should be addressed to Bo Gao, surfgao@yahoo.com.cn

Received 30 November 2012; Accepted 8 December 2012

Academic Editor: Jianxin Zou

Copyright © 2012 Bo Gao et al. This is an open access article distributed under the Creative Commons Attribution License, which permits unrestricted use, distribution, and reproduction in any medium, provided the original work is properly cited.

Four techniques using high-current pulsed electron beam (HCPEB) were proposed to obtain surface nanostructure of metal and alloys. The first method involves the distribution of several fine Mg nanoparticles on the top surface of treated samples by evaporation of pure Mg with low boiling point. The second technique uses superfast heating, melting, and cooling induced by HCPEB irradiation to refine the primary phase or the second phase in alloys to nanosized uniform distributed phases in the matrix, such as the quasicrystal phase $\text{Mg}_{30}\text{Zn}_{60}\text{Y}_{10}$ in the quasicrystal alloy $\text{Mg}_{67}\text{Zn}_{30}\text{Y}_3$. The third technique involves the refinement of eutectic silicon phase in hypereutectic Al-15Si alloys to fine particles with the size of several nanometers through solid solution and precipitation refinement. Finally, in the deformation zone induced by HCPEB irradiation, the grain size can be refined to several hundred nanometers, such as the grain size of the hypereutectic Al-15Si alloys in the deformation zone, which can reach ~ 400 nm after HCPEB treatment for 25 pulses. Therefore, HCPEB technology is an efficient way to obtain surface nanostructure.

1. Introduction

Nanomaterials are typically characterized by ultrafine grains [1]. They fundamentally possess several unique properties and behavior such as increased strength/hardness, enhanced diffusivity, enhanced thermal expansion coefficient, and superior soft magnetic properties [2] compared with the conventional coarse-grained materials. With continuous discovery of the unique properties of nanomaterials in recent years, various processing techniques have been developed to synthesize bulk nanomaterials, such as ultrafine powder consolidation [3], amorphous solid crystallization [4], ball milling [5], and severe plastic deformation [6].

High-current pulsed electron beam (HCPEB) technique, as a novel and valid method [7, 8] used for material surface modification, is long considered to be a very simple, reliable, and highly efficient method. The electron beam generates intense and superfast melting, evaporation, solidification, and even ablation on the surface of target materials together with the formation of thermal stress and shock waves. Therefore, the depth of the HCPEB modification zone can reach several hundred micrometers [9–12], which greatly

satisfies the modification demands for engineering materials. The combination of these influencing factors, peculiar to HCPEB treatment, can lead to the nanocrystalline formation in near-surface layers of metallic materials [13, 14].

Hence, four methods involving HCPEB technology were proposed to obtain surface nanocrystalline formation in this paper.

2. Experimental Procedures

2.1. Starting Materials and HCPEB Treatment. The starting materials in this experiment were pure Mg (99.7 wt%), $\text{Mg}_{67}\text{Zn}_{30}\text{Y}_3$ quasicrystal alloy (with a chemical composition of Zn (50.86 wt%), Y (7.02 wt%), and Mg balance), and hypereutectic Al-15Si alloy (with chemical composition of Si (15 wt%) and Al balance). Prior to HCPEB treatment, the samples were cut into $\Phi 10 \text{ mm} \times 9 \text{ cm}$ cylinders, with surfaces that were mechanically polished and washed by absolute ethyl alcohol. Then, the sample surfaces were treated through “Nadezhda-2” type HCPEB system, with the following working parameters: accelerating voltage, 23 kV;

energy density, 1 J/cm^2 to 3 J/cm^2 ; pulse duration, $\sim 1 \mu\text{s}$; and pulse number, 10 for pure Mg and quasicrystal alloy $\text{Mg}_{67}\text{Zn}_{30}\text{Y}_3$ and 25 for hypereutectic Al-15Si alloy.

2.2. Microstructural Analysis. The sample surface and cross-section morphologies were analyzed using a field emission gun scanning electron microscope (SEM) (Jeol JSM 6500 F) with EBSD acquisition camera and Channel 5 software. The beam control mode was applied for automatic orientation mapping with a step size of $0.04 \mu\text{m}$. Thin films for transmission electron microscopy (TEM) were prepared by grinding, dimpling, and ion-beam thinning, and the microstructure characteristics were observed in a transmission electron microscope (FEI-Tecna G220).

3. Results and Discussion

The characteristics of the obtained nanostructures according to the four techniques using HCPEB treatment are discussed as follows.

3.1. Surface Characteristics of Pure Mg after HCPEB Treatment. Figure 1 illustrates the surface SEM morphology of HCPEB-treated pure Mg for 10 pulses under energy density of 3 J/cm^2 . Several separated bulges are evident, and numerous fine particles were observed between and on top of these bulges. The chemical composition of the fine particles is determined to be pure Mg using EDS analysis, and the size of the fine particles ranges from several hundred nanometers to several micrometers. Pure Mg vaporizes on the top surface of the treated sample. The special morphology formation can be explained as follows. First, the surface temperature of the HCPEB-treated Mg reaches boiling point, vaporization occurs at a given depth determined by the energy density of HCPEB, and a considerable amount of bubbles form in the liquid Mg solution. Second, when the bubbles reach the top surface, the abruption of these bubbles induces shock effect on the nearby zone and a large number of fine particles will erupt simultaneously. Finally, these fine erupted particles fall to the top frozen surface under the effect of gravity, and the special surface morphology as seen in Figure 1 is formed.

Thus, vaporization behavior induced by HCPEB treating low-boiling point metal can produce abundant fine particles with sizes ranging from several hundred nanometers to several micrometers.

3.2. Microstructure Characteristics of $\text{Mg}_{67}\text{Zn}_{30}\text{Y}_3$ Quasicrystal Alloy before and after HCPEB Treatment. Figure 2 demonstrates the surface back-scattered electron (BSE) images of $\text{Mg}_{67}\text{Zn}_{30}\text{Y}_3$ quasicrystal alloy in the initial state and after HCPEB treatment for 10 pulses. Figure 2(a) depicts the initial microstructure characteristics of $\text{Mg}_{67}\text{Zn}_{30}\text{Y}_3$ quasicrystal alloy, consisting of gray matrix phase Mg_7Zn_3 , black dendrite α -Mg phase, and white petal-shaped quasicrystal $\text{Mg}_{30}\text{Zn}_{60}\text{Y}_{10}$ phase [15]. The phase contrast change is mainly attributed to the different contents of Mg element in the different phases. Two types of dendrites are both Mg-rich phases and have few solid solution of Y element. By contrast,

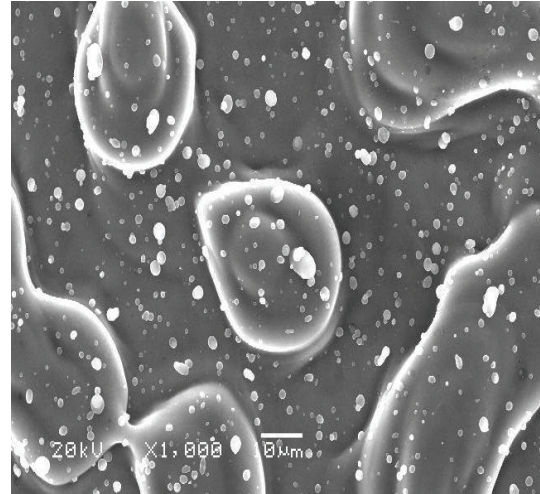


FIGURE 1: Surface SEM morphology of HCPEB-treated pure Mg with 10 pulses under energy density of 3 J/cm^2 .

the white petal-shaped phase consists of the following: Mg, 37.496%; Zn, 53.022%; and Y, 9.482%. Although a certain deviation from the quasicrystal $\text{Mg}_{30}\text{Zn}_{60}\text{Y}_{10}$ phase in standard ternary Mg-Zn-Y alloy is reported in [13], the phase should be the quasicrystal $\text{Mg}_{30}\text{Zn}_{60}\text{Y}_{10}$ from the typical petal morphology, and the deviation is probably caused by the EDS test error. Figure 2(b) illustrates the typical surface morphology of $\text{Mg}_{67}\text{Zn}_{30}\text{Y}_3$ quasicrystal alloy after HCPEB treatment for 10 pulses. The phase boundaries between different phases become clear, and the coarse petal phase disappears. During multiple HCPEB treatments, the top surface of the treated sample undergoes repeated melting and solidification. The chemical composition tends to distribute uniformly as a result of the chemical composition diffusion during the HCPEB process, forming the special morphology (Figure 2(b)). However, determining the accurate size of the quasicrystal $\text{Mg}_{30}\text{Zn}_{60}\text{Y}_{10}$ phase after 10-pulse treatment by SEM observation is quite difficult.

Figures 2(c) and 2(d) illustrate the TEM observations of the quasicrystal phase of the $\text{Mg}_{67}\text{Zn}_{30}\text{Y}_3$ quasicrystal alloy before and after HCPEB treatment. Figure 2(c) demonstrates the TEM bright field image of the initial sample and corresponding SAED pattern (five-fold symmetry). A black petal-shaped phase is observed under TEM view. Through the identification of the SAED pattern with five-fold symmetry, the petal-shaped phase is considered as quasicrystal $\text{Mg}_{30}\text{Zn}_{60}\text{Y}_{10}$ with icosahedral structure of quasiperiodic structure arrangement. This result further confirms the observations obtained from SEM. In addition, several fine branches are formed in the vicinity of the large petal-shaped quasicrystal phase, known as the two-fold axis of quasicrystal growth. Figure 2(d) illustrates the TEM bright field image of a 10-pulse-treated sample and corresponding SAED pattern (diffraction rings). After HCPEB treatment for 10 pulses, a considerable amount of nanosized particles with grain size of approximately 10 nm to 30 nm is uniformly distributed in surface layer. The interplanar

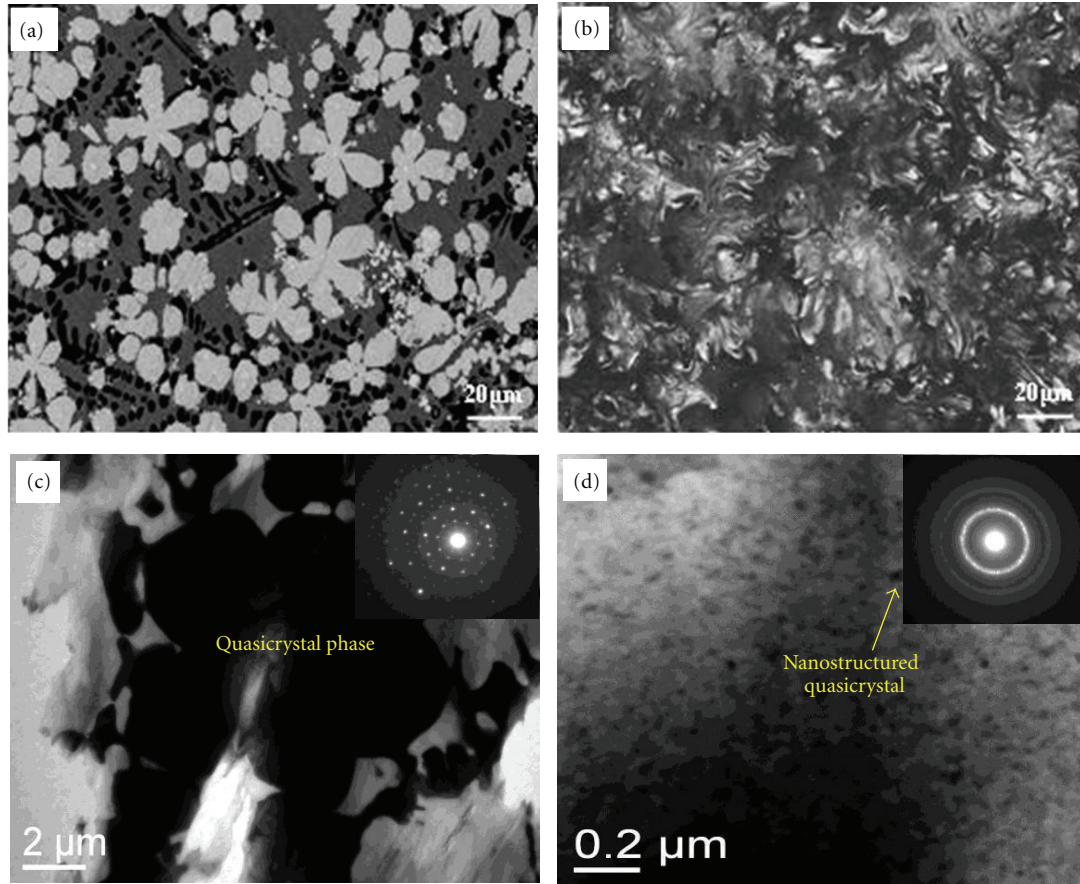


FIGURE 2: SEM and TEM morphology of quasicrystal $\text{Mg}_{67}\text{Zn}_{30}\text{Y}_3$ alloy before and after HCPEB treatment under energy density of $\sim 2.5 \text{ J/cm}^2$ and 10 pulses (SEM morphology of quasicrystal $\text{Mg}_{67}\text{Zn}_{30}\text{Y}_3$ alloy (a) before and (b) after HCPEB treatment, TEM morphology of quasicrystal phase (c) in initial sample and corresponding SAED pattern, (d) in treated sample and corresponding SAED pattern).

spacing values corresponding to each diffraction ring were calculated and compared with interplanar spacing (d_{stan}) values of acknowledged quasicrystal $\text{Mg}_{30}\text{Zn}_{60}\text{Y}_{10}$. Hence, the dispersed metastable nanocrystalline phase is identified to be the quasicrystal phase $\text{Mg}_{30}\text{Zn}_{60}\text{Y}_{10}$. Thus, a melted layer containing a large number of nanostructured quasicrystal phases is obtained by the HCPEB treatment.

Hence, using HCPEB multiple bombardments, the coarse petal quasicrystal phase $\text{Mg}_{30}\text{Zn}_{60}\text{Y}_{10}$ can be refined to dispersed distribution nanostructured quasicrystal phase.

3.3. Microstructure Characteristics of Hypereutectic Al-15Si Alloy before and after HCPEB Treatment. Figure 3 depicts the SEM surface morphology of hypereutectic Al-15Si alloy before and after HCPEB treatment under energy density of $\sim 3 \text{ J/cm}^2$. For the initial sample shown in Figure 3(a), the Al-Si eutectic structure in as-cast hypereutectic Al-15Si alloy is clearly observed by SEM. In addition, a small number of coarse primary Si phases with size of several ten micrometers are distributed randomly on the surface. For the 25 pulse-treated sample shown in Figure 3(b), the eutectic structure disappears completely after HCPEB treatment and numerous cellular cells ($\sim 100 \text{ nm}$ wide) are uniformly distributed

on the top surface. Additionally, a remarkable amount of Si nanoparticles is precipitated on the boundary of the nanocellular cell structure. Most of the eutectic Si phase of initial sample solid dissolves in the $\alpha\text{-Al}$ and forms the supersaturated solid solution. Some of the Si element precipitate from the supersaturated solid solution during the rapid solidification. The estimated size of the Si nanoparticles ranges from 5 nm to 50 nm. Thus, the size of eutectic Si phase can be refined to 5 ~ 50 nm after HCPEB treatment.

This process is the third way to obtain nanostructure by solid solution and precipitation refinement induced by HCPEB treatment.

3.4. Microstructure Characteristics of Deformation Zone of HCPEB-Treated Hypereutectic Al-15Si Alloy. A deformation zone can be found under the melted layer of the HCPEB-treated sample, but few studies on the grain size distribution in this zone have been reported. Figure 4(a) illustrates the SEM morphology image of this deformation zone (distance from the top surface approximately from $10 \mu\text{m}$ to $30 \mu\text{m}$). Several fine Si particles are distributed in this zone, and the initial eutectic Si phases are deduced to be transformed to

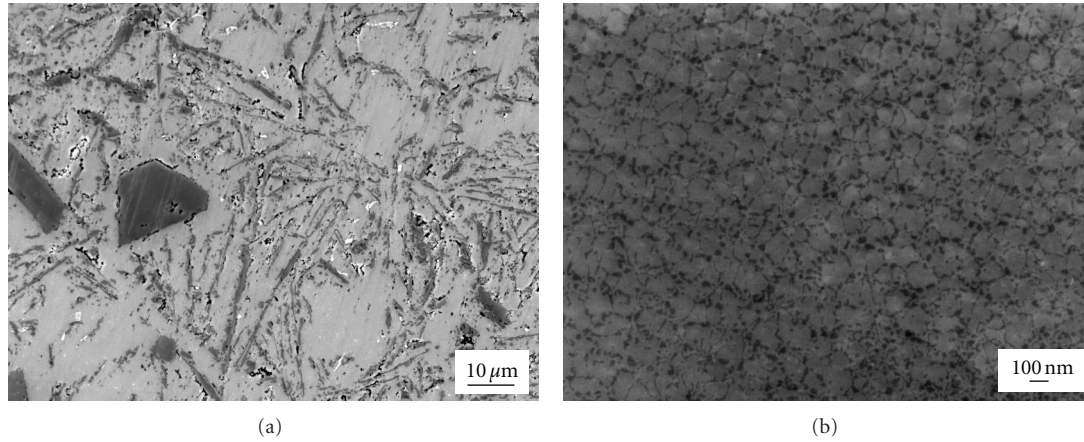


FIGURE 3: SEM surface morphology of hypereutectic Al-15Si (a) before HCPEB treatment and (b) after 25-pulse treatment under energy density of $\sim 3 \text{ J/cm}^2$.

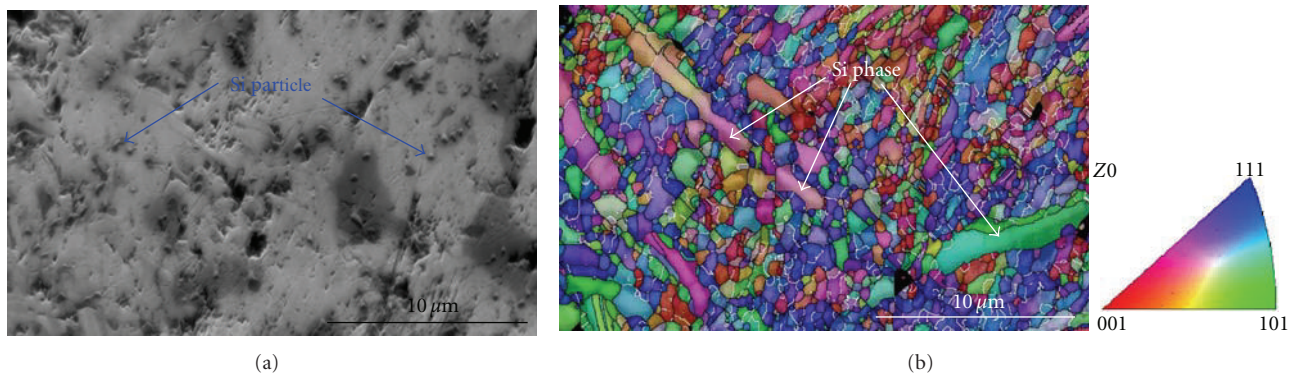


FIGURE 4: Cross-section morphology of HCPEB-treated hypereutectic Al-15Si alloy heat-affected zone for 25 pulses (a) and corresponding EBSD orientation map.

these fine particles as a result of microplastic deformation induced by multiple HCPEB shock wave impacts. From the corresponding EBSD orientation map (Figure 4(b)), several large lamellar primary Si phases were subdivided into several grains under multiple plastic deformations induced by the shock wave, and some Si phases release coupled stress as seen in Figure 4(b) and refined to several hundred nm. For the Al matrix, the grains were transformed from coarse dendrite crystal to fine equiaxed crystal with size of $\sim 300 \text{ nm}$ (Figure 4(b)). And the preferred orientation for Al phase in this zone is $[111]$ direction, which is parallel to propagation direction of shock wave.

To show the grain distribution clearly, Figure 5(a) illustrates the EBSD grain map, white lines present the low angel grain boundary (grain orientation difference between 3° and 10°), and black lines present the high angel grain boundary (orientation difference over 10°). Figure 5(b) provides the corresponding grain size distribution map in this zone with an orientation difference of over 3° . Figure 5(a) shows that numerous low-angel grain boundaries are formed resulting from severe plastic deformation induced by the HCPEB shock wave impact. Most of the grains are less than $1 \mu\text{m}$ in size, and the average grain size is approximately 460 nm from

statistical result of all the grain sizes in the deformation zone (Figure 5(b)).

Hence, the grain size in the deformation zone under melted layer can reach several hundred nanometers after multiple pulses treatment of HCPEB. This is the fourth way to obtain a nanostructure by HCPEB treatment.

4. Conclusions

This work investigated the different techniques involving HCPEB treatment to obtain nanostructure for pure Mg, quasicrystal Mg alloy $\text{Mg}_{67}\text{Zn}_{30}\text{Y}_3$, and hypereutectic Al-15Si alloy. The main results are as follows.

- (1) A considerable amount of fine particles with sizes from several hundred nanometers to several micrometers are distributed on the top surface of treated pure Mg sample as a result of vaporization behavior induced by HCPEB treating.
- (2) After 10 pulses of HCPEB treatment for quasicrystal Mg alloy $\text{Mg}_{67}\text{Zn}_{30}\text{Y}_3$, the phase boundaries between different phases become more apparent because of repeated melting and solidification. The surface

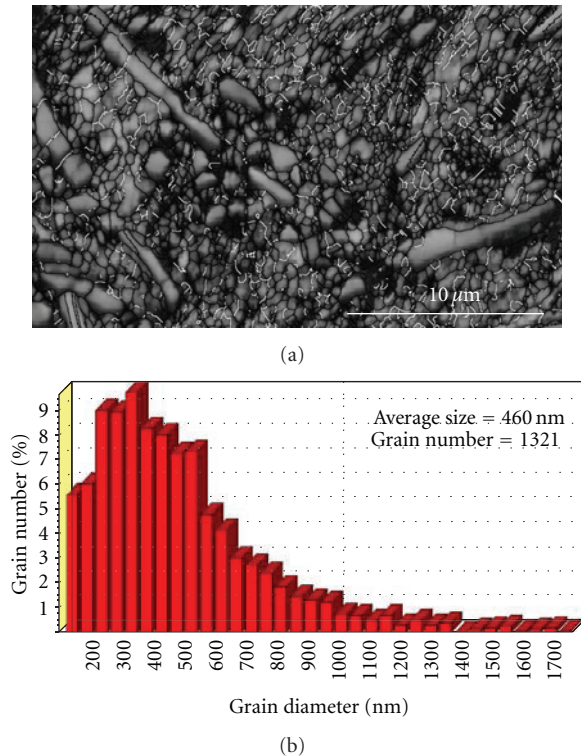


FIGURE 5: EBSD grain map of HCPEB-treated hypereutectic Al-15Si alloy heat-affectation zone for (a) 25 pulses and (b) corresponding grain size distribution under grain orientation difference of over 3° .

chemical composition tends to be homogeneously distributed. A large number of nano quasicrystal $\text{Mg}_{30}\text{Zn}_{60}\text{Y}_{10}$ phases are formed with size of approximately 10 nm to 30 nm.

- (3) After 25 pulses of HCPEB treatment for hypereutectic Al-15Si alloy, many cellular cells with ~ 100 nm diameter are uniformly distributed on the top surface. In addition, a number of Si nanoparticles (5 nm to 50 nm) are precipitated on the boundary of the nanocellular cell structure.
- (4) After 25 pulses of HCPEB treatment for hypereutectic Al-15Si alloy, the grain size in the deformation zone induced by multiple HCPEB shock wave impacts can reach several hundred nanometers.

Acknowledgments

The authors would like to acknowledge the support from the Fundamental Research Funds for the Central Universities (N090602009 and N100402010) and the key projects in the National Science & Technology Pillar Program during the eleventh five-year plan period (2009BAE80B01).

References

- [1] G. Liu, J. Lu, and K. Lu, "Surface nanocrystallization of 316L stainless steel induced by ultrasonic shot peening," *Materials Science and Engineering A*, vol. 286, no. 1, pp. 91–95, 2000.

- [2] C. Suryanarayana, "Nanocrystalline materials," *International Materials Reviews*, vol. 40, no. 2, pp. 41–64, 1995.
- [3] X. Zhang, H. Wang, M. Kassem, J. Narayan, and C. C. Koch, "Preparation of bulk ultrafine-grained and nanostructured Zn, Al and their alloys by in situ consolidation of powders during mechanical attrition," *Scripta Materialia*, vol. 46, no. 9, pp. 661–665, 2002.
- [4] T. Nagase, M. Nakamura, and Y. Umakoshi, "Electron irradiation induced nano-crystallization in $\text{Zr}_{66.7}\text{Ni}_{33.3}$ amorphous alloy and $\text{Zr}_{60}\text{Al}_{15}\text{Ni}_{25}$ metallic glass," *Intermetallics*, vol. 15, no. 2, pp. 211–224, 2007.
- [5] T. P. Yadav, N. K. Mukhopadhyay, R. S. Tiwari, and O. N. Srivastava, "Studies on the formation and stability of nano-crystalline $\text{Al}_{50}\text{Cu}_{28}\text{Fe}_{22}$ alloy synthesized through high-energy ball milling," *Materials Science and Engineering A*, vol. 393, no. 1-2, pp. 366–373, 2005.
- [6] M. N. Ahmadabadi, H. Shirazi, H. Ghasemi-Nanesa, S. H. Nedjad, B. Poorganji, and T. Furuha, "Role of severe plastic deformation on the formation of nanograins and nano-sized precipitates in Fe-Ni-Mn steel," *Materials and Design*, vol. 32, no. 6, pp. 3526–3531, 2011.
- [7] S. Hao, P. Wu, J. Zou, T. Grosdidier, and C. Dong, "Microstructure evolution occurring in the modified surface of 316L stainless steel under high current pulsed electron beam treatment," *Applied Surface Science*, vol. 253, no. 12, pp. 5349–5354, 2007.
- [8] T. Grosdidier, J. X. Zou, N. Stein, C. Boulanger, S. Z. Hao, and C. Dong, "Texture modification, grain refinement and improved hardness/corrosion balance of a FeAl alloy by pulsed electron beam surface treatment in the "heating mode"," *Scripta Materialia*, vol. 58, no. 12, pp. 1058–1061, 2008.
- [9] J. X. Zou, K. M. Zhang, S. Z. Hao, C. Dong, and T. Grosdidier, "Mechanisms of hardening, wear and corrosion improvement of 316 L stainless steel by low energy high current pulsed electron beam surface treatment," *Thin Solid Films*, vol. 519, no. 4, pp. 1404–1415, 2010.
- [10] Y. Qin, C. Dong, Z. F. Song et al., "Deep modification of materials by thermal stress wave generated by irradiation of high-current pulsed electron beams," *Journal of Vacuum Science & Technology A*, vol. 23, pp. 430–435, 2009.
- [11] J. X. Zou, T. Grosdidier, K. M. Zhang, B. Gao, S. Z. Hao, and C. Dong, "Microstructures and phase formations in the surface layer of an AISI D2 steel treated with pulsed electron beam," *Journal of Alloys and Compounds*, vol. 434–435, pp. 707–709, 2007.
- [12] J. Zou, T. Grosdidier, K. Zhang, and C. Dong, "Mechanisms of nanostructure and metastable phase formations in the surface melted layers of a HCPEB-treated D2 steel," *Acta Materialia*, vol. 54, no. 20, pp. 5409–5419, 2006.
- [13] Q. F. Guan, H. Zou, G. T. Zou et al., "Surface nanostructure and amorphous state of a low carbon steel induced by high-current pulsed electron beam," *Surface and Coatings Technology*, vol. 196, no. 1–3, pp. 145–149, 2005.
- [14] Y. Hao, B. Gao, G. F. Tu, S. W. Li, C. Dong, and Z. G. Zhang, "Improved wear resistance of Al-15Si alloy with a high current pulsed electron beam treatment," *Nuclear Instruments and Methods in Physics Research B*, vol. 269, no. 13, pp. 1499–1505, 2011.
- [15] A. P. Tsai, A. Inoue, and T. Masumoto, "Stoichiometric icosahedral phase in the ZnMgY system," *Journal of Materials Research*, vol. 12, pp. 1468–1471, 1997.

